Estimation of the diffusion coefficient of hygroscopic materials using a contactless transient *THz* water vapour content imaging and excitation device

M. Bensalem [a,*], A. Sommier [b], J.C. Mindeguia [b], J.C. Batsale [b], C. Pradere [a]

[a] *Département Recherche & Innovation, Epsyl - Groupe ALCEN, Talence 33405, France*
[b] *I2M, UMR CNRS 5295, 351 cours de la libération, Talence 33405, France*

Contactless monitoring
Terahertz technique
Diffusion coefficient
Image processing
Mass transfer modelling
Inverse method

A B S T R A C T

The investigation of humidity movement during drying or imbibition processes represents a serious challenge for several industries, such as the wood-based material industry and paper industry. Recently, several studies have been conducted on the efficiency contactless Terahertz technique (*THz*) to map the water content. In this study, this technique based on coupling infrared camera and developed Tera-Thermo-Converter, is used for the estimation of mass diffusion coefficient within hygroscopic materials initially dry. A water vapour water content excitation device is designed to excite the samples in a *THz* semitransparent enclosure during the monitoring. The recorded infrared films showed a pronounced mitigation of the signal over time, indicating penetration of vapour through the sample. Processing image techniques such as the four-image, algorithm and Singular Value Decomposition (*SVD*) and averaging are used to obtain the space-time water content map. A simplified one-dimensional model of mass transfer is proposed to estimate the diffusion coefficient using two inverse methods: a) a statistical method based on Bayesian approach, and b) a minimization method based on Levenberg–Marquardt algorithm (*LM*). The results showed that *THz* imaging technique coupled with the appropriate processing and the adequate modelling, is able not only to map the water content field but also to monitor the transient transfer and estimate the diffusion coefficient without contact.

1. Introduction

In the industries of hygroscopic materials such as wood and paper, the control of water content is a crucial step that directly affects the final quality of the product. The water movement within materials is often coupled to their mechanical behaviour. Thus, local measurement is necessary for obtaining reliable products. Therefore, simulations of the humidity movement within samples must be accomplished by experimental measurements (Clouet et al. [1] and Clouet [2]). Conventional techniques such as global monitoring of water content weight through weighting the sample at dry and wet case, provide only global information, such as global water content. Access to reliable monitoring of saturation profiles at the local scale inside a porous medium requires a more sophisticated imaging technique. Due to the opacity feature of water (vapour or liquid) to noninvasive techniques, radiative and magnetic techniques represent effective tools allowing the detection of water within porous media. This is due to the attenuation of the signal crossing the water. In the literature, several techniques have been used in the context of water content monitoring. These techniques can be classified as nuclear radiation methods (such as neutron imaging) or electromagnetic radiation methods (such as X rays, gamma rays, infrared waves, and terahertz waves). Electromagnetic techniques can also be classified by the danger represented to the operators depending on the wavelength range. The waves can be ionizing radiation, such as gamma rays or X rays, or nonionizing radiation, such as infrared or *THz* radiation.

Early techniques used gamma rays or X rays, which are harmful to humans. Computed tomography based on the X-rays technique has been used in the context of water content monitoring, such as monitoring the local water content in wood in the steady-state case (Dvinskikh et al. [3]), visualizing the influence of the microstructure of wood on water movement (Derome et al. [4]), and checking the displacement of water content in preferential directions (Sandberg [5] and Zillig [6]). Moreover, magnetic resonance imaging (*MRI*) is also used as a contactless technique to locally estimate the water content within wood under different con-

* Corresponding author.
E-mail address: mbensalem.cnd@gmail.com (M. Bensalem).

https://doi.org/10.1016/j.ijheatmasstransfer.2023.124064

Abbreviations & symbols

Abbreviation

THz	Terahertz
TTC	TeraThermo-Converter
PTFE	Polytetrafluoroethylene
RH	Relative humidity
IR	Infrared
SVD	Singular value decomposition

Symbols

Tr	Transmittance (-)
$\overline{Tr}$	Average transmittance (-)
I	Transmitted signal (amplitude) (DL)
I_0	Emitted signal (amplitude) (DL)
l	height of images along the y-axis
t	time (s)
x, y, z	Space dimensions (m)
A	absorbence (-)
ρ_s	Density of sample (kg/m^3)
ρ_w	Density of water (kg/m^3)
μ_s	Absorption coefficient of solid (m^{-1})
μ_w	Absorption coefficient of water (m^{-1})
l_s	Thickness of sample (m)
W	Water content field (kg of water $kg^{-1}$of solid)
D_z	Diffusion coefficient along the z-axis (m^2/s)
D_y	Diffusion coefficient along the y-axis (m^2/s)
W_s	Water content at $z = 0$ in the boundary condition (kg of water $kg^{-1}$of solid)
W_0	Water content at $t = 0$ in the boundary condition (kg of water $kg^{-1}$of solid)
W_∞	Water content at $z = \infty$ in the boundary condition (kg of water $kg^{-1}$of solid)
$\bar{W}$	Average water content (-)
$\bar{W}_{exp}$	Average experimental water content (-)
$\bar{W}_{rec}$	Average reconstructed (modelled) water content (-)
P	Probability density (prior or posterior)
α	Parameter to estimate in Bayesian approach
D_i	Diffusion coefficient base (m^2/s)
f_{prob}	Probability function
D_{Bayes}	Diffusion coefficient estimated by Bayesian approach (m^2/s)
β	Parameter to estimate by minimization
$Y_{i,j}$	Experimental data in the minimization model
f	Modelled function in the minimization model
δ	Variation in the parameter β
$S(\beta)$	Sum of square error in the minimization model
$J_{i,j}$	Jacobian matrix
λ	Damping factor
D_0	Initial parameter (diffusion coefficient) given to the algorithm (m^2/s)
D_{minim}	Diffusion coefficient estimated by Levenberg–Marquardt algorithm (m^2/s)
m	Mean value of error
σ	Standard deviation of error

ditions (Hameury and Sterley [7], MacMillan et al. [8] and Ekstedt et al. [9]). A recent technique called neutron imaging (*NI*) has also been implemented as a contactless technique in water content estimation and has shown interesting results (Gilani et al. [10] and Gilani et al. [11]), which allowed the validation of a hygro-thermomechanical model for wood (Abbasion et al. [12]). Despite the interest in these techniques, they can include certain obstacles, making their use in industry complicated. The techniques can be harmful, expensive, or difficult to implement in industrial production lines. Accordingly, a contactless technique based on terahertz waves is proposed here to study the dynamics of water content (transient case) within a porous medium and estimate the diffusion coefficient.

Terahertz waves represent nonionizing electromagnetic waves situated between infrared waves and microwaves and often abbreviated *THz*. Their wavelength situated between 30 μm and 3000 μm. The terahertz technique is safe and inexpensive and requires no particular precaution. These waves penetrate insulating materials up to a few centimetres, but they are absorbed by water. This limitation makes terahertz technology a reliable tool for many applications, such as Non-destructive testing (*NDT*), inspection and mainly water content monitoring. The terahertz technique was used to study different materials, such as paper quality during the drying process (Banerjee et al. [13]), monitoring the water content within leaves without contact (Hadjiloucas et al. [14], Zhang et al. [15], Gente et al. [16] and Santesteban et al. [17]), and estimating the absorption coefficient within wood (Jördens et al. [18] and Piesiewiczet et al. [19]). This technique has also been used to estimate the temperature without contact with polymers (Bensalem et al. [20]). The study of mass transfer within hygroscopic materials has often been conducted on two aspects: (a) the analysis of the water content field and (b) the estimation of the diffusion coefficient during mass transfer (drying or imbibition). In this context, imaging techniques were mostly conducted on the first aspect, where relations between global water content and signal attenuation can be established. Several studies have been performed on the estimation of the diffusion coefficient (Mukam Fotsing and Tchagang [21]), where the diffusion coefficient in different directions has been determined. This coefficient was also determined using Fick's Law with known values of water content change, distance to the drying source and drying time (Yasushi [22]). Some studies consider the water content dependency of the diffusion coefficient (Koponen [23]), which can greatly improve the value obtained. The minimization method is used to find the diffusion coefficient of the water content profile obtained by the X-rays technique and computed by the finite element method (Eriksson et al. [24]). Another numerical method based on finite difference is used to numerically determine the diffusion coefficient within wood (Liu et al. [25]). The infinite Fourier series solution to the one-dimensional Fick equation is used to estimate the diffusion coefficient in the unsteady-state case (Peralta and Bangi [26]).

This study represents a complementary study of (Bensalem et al. [27]) and is directed to the second aspect of Fickian diffusion coefficient estimation. The diffusion coefficient of hygroscopic materials represents the ratio of flux density to the opposite of the concentration gradient in the diffusion direction is a common definition for the diffusion coefficient (Animasaun et al. [28]). The efficiency of the *THz* technique based on a Tera-Thermo-Converter *TTC* coupled with a vapour excitation device is investigated. *TTC* represents a tool developed within the institute of mechanics of Bordeaux (*I2M*) allowing the transformation of terahertz waves to an infrared signal directly captured by an infrared camera (Romano et al. [29]). Herein, the developed measurement system settings are detailed for the first time. The transfer function found in (Bensalem et al. [27]) based on the Beer–Lambert law and linking the absorbence to the water content is used to obtain the experimental absolute water content field (kg of water per kg of material). Thereafter, the obtained infrared films (raw data) are processed using different algorithms to extract the appropriate data, denoise the information and integrate the convenient model based on Fick law and simple boundary conditions. The estimation of the diffusion coefficient is based on two approaches: (a) statistic using Bayesian probability function and (b) an inverse method based on a minimization between experimental and modelled

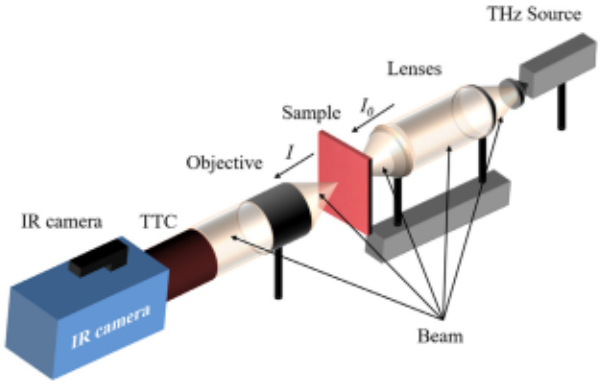

Fig. 1. Terahertz system consisting of an infrared camera, *TTC*, sample, optical system and *THz* source.

fields of normalized water content using the Levenberg–Marquardt algorithm.

2. Materials and processing method

In this study, the terahertz system used represents the same system used in (Bensalem et al. [20]). An important point here is the development of an excitation device that ensures not only the water vapour excitation of the sample, but also control of the space form, amplitude and time form of excitation. Indeed, the excitation about to be realized can have several special forms analogous to the thermal excitation used in thermography infrared: a point-like form, linear form or homogeneous excitation at the surface of the sample. On the other hand, the temporal form of the excitation can also be controlled, such as a Dirac pulse, Heaviside, step, etc. However, the temporal form of excitation should consider the diffusion characteristic time of mass transfer. This means, for example, that a mass pulse can last one hour. In addition, the control of the amplitude of excitation or the intensity can be obtained through the control of saturation of vapour used in the excitation.

In this study, the excitation is limited to one intensity, one space form and one time form and is detailed in paragraph 2.1.3.

2.1. Materials

2.1.1. THz measurement system

The imaging setup based on a patented *THz*-to-*IR* focal plane array sensor aiming to carry out contactless measurements of the water consists of five components: (i) a *THz* Gunn diode, (ii) an optical system, (iii) an infrared camera that can be considered the *2D* detector, (iv) a *TTC* and (v) a modulator.

- The *THz* source used comprises a Gunn diode with a power of 200 *mW* and a frequency of 110 *GHz* or wavelength of 2.7 *mm*.
- The optical system in this experiment consists of a beam expander (f in Fig. 1) composed of two 110-*mm*-diameter plano-convex lenses made of *PTFE* (THORLABS) with a focal distance of 100 *mm* and an objective (c) composed of three Teflon™ lenses designed by Alphanov. The objective situated between the sample and the detector aims to image the sample on the *TTC*, according to different magnifications.
- The camera used in this study (FLIR SC7000) is a mid-wave indium antimonide (*InSb*) quantum detector-based infrared camera with a spectral band of 3.5 μm–5.15 μm and acquisition frequencies up to 1 *kHz*. The detector's matrix size is 256 *px* x 320 *px* with a minimum spatial resolution of 25 $\mu m/px$. This camera can achieve a frame rate (acquisition frequency) of up to 800 images/*s* in snapshot mode (when the matrix detectors work concurrently).

It is important to note that several optical deviations, such as beam deformation, inhomogeneity due to optical misalignment or the diffraction phenomenon, are present. This led us to develop image processing methods to extract the appropriate data pixel by pixel. The scheme of the *THz* setup used in this study is shown in Fig. 1.

The thermal noise linked to the use of a thermal detector can be avoided through modulation of the signal. The modulation of the *THz* beam coupled with image processing allows a decrease in the thermal noise resulting from the in-plane thermal diffusion on the *TTC*.

It is worth noting that in the experiment, the sample shown in Fig. 1 will be replaced by the *THz*-semitransparent enclosure containing the sample and connected to a vapour excitation system.

2.1.2. Sample preparation and material conditioning

Blotting paper is a homogeneous one-constituent material that is often used to absorb excess liquid substances by capillary action. It is mainly composed of cellulose and a mixture of sulfite without a charge, glue, or mechanical primer. Since cellulose represents one of the main constituents of wood, blotting paper represents a good homogeneous sample on which to perform standard tests, calibration and validation methods by *THz* imaging.

The investigated sample consists of 10 stacked blotting papers (CANSON 160 *mm* x 210 *mm*, density of 125 g/m^2) with a size of 30 *mm* x 20 *mm* x 0.2 *mm*. First, the samples are dried for 24 *h* in an oven at 105 °*C* to constant mass. The hydric excitation of the sample is performed via saturated vapour inside a container of saline solution allowing the generation of wet air at a given relative humidity *RH*. The resulting *RH* is measured by a contactless sensor (Tinytag plus 2) placed inside the container. An integrated manual pump connected to the container allows the generation of a pressure gradient inside the container, promoting vapour movement within the container.

Through a tube and aquarium pump, the container was connected to the enclosure housing the dry blotting paper sample. Through the use of the pump, the vapour travels from the container to the enclosure, excites the sample, and then returns to the container.

The high-frequency infrared camera used allows hundreds of full-field images to be obtained per second, which gives detailed information about the transfer. This allows better monitoring of the water content over time; for example, in a scan of a region of interest of 40 *px* x 30 *px*, 190 infrared films over 16 *h* can be obtained by recording films of only 1 *s* every 5 min. The samples and excitation device used are shown in Fig. 2.

2.1.3. Hydric excitation device

Similar to the thermal excitation methods commonly used to measure the thermal diffusion coefficient of materials (for example, the flash method (Parker et al. [30])), the main objective of the developed hydric excitation device is to establish fixed hydric conditions. This is through a one-dimensional circulation of wet air with known *RH* and flow rate on a defined boundary of the sample supposed initially dry.

The sample that represents 10 stacked blotting papers is placed between two plastic enclosures semitransparent to the *THz* frequency range. A rubber strip is placed on the three sides of the sample edges to avoid absorption or escape of water content. The only side of the sample that is not sealed is exposed to a continuous vapour flow. The wet air flow was induced at low velocity by an aquarium pump (*EHEIM* air pump 100 with a maximum flow rate of 100 *l/h* and a pressure of 200 *mbar*). The *RH* of the wet air is

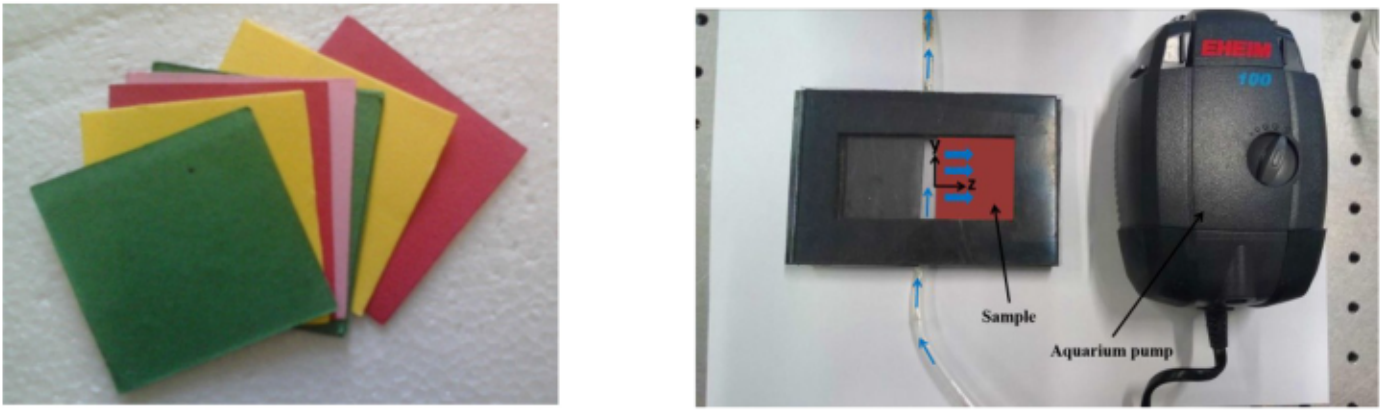

Fig. 2. (a) Stacked samples of blotting paper, and (b) hydric excitation setup: insulated semitransparent enclosure and aquarium pump.

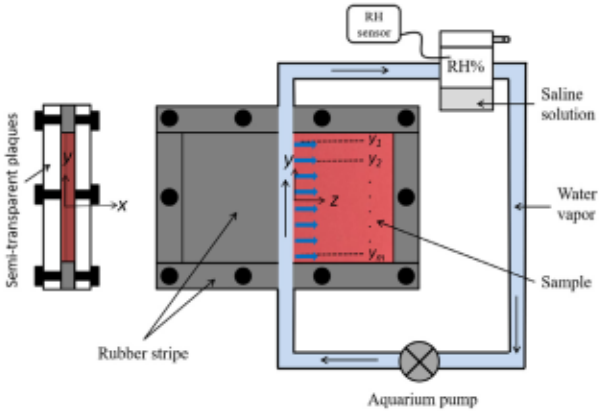

Fig. 3. Hydric excitation setup consists of a semitransparent enclosure, a pump, a rubber insulator, and a wet air container.

chosen to be maximum (97%) to promote the mass transfer thanks to a saline solution placed in the air circuit and controlled during the experiments by an *RH* sensor. The saline solution is kept inside the vacuum container to stabilize the *RH* at 97%. It is obtained by dissolving the salt potassium sulfate K_2SO_4 in distilled water in the container. The sample is then imaged for 16 *h* (films of 1 *s* duration or every 5 min). Once the films are recorded, image processing using the four-image method and singular value decomposition *SVD* decomposition is carried out thanks to MATLAB®. The hydric excitation device is shown in Fig. 3.

As mentioned previously, when the sample is dry, it is placed inside the excitation device on the sample enclosure for the experiment. The pump is turned on to continuously pump saturated wet air with *RH* 97%. The acquisition of the transmitted signal is started by the infrared camera with a frequency of 200 *Hz* (200 images per second). Infrared films of 1 *s* were recorded automatically every 5 min for 16 *h*.

On the other hand, synchronization of the excitation and acquisition frequencies allows imaging of the excitation and response phases of the *TTC* over time. A two-channel waveform generator (Agilent 33500B Series) is used to synchronize the *THz* source ignition and camera acquisition (Bensalem et al. [27]).

The generator also allows modulation of the power of the *THz* beam to limit thermal diffusion in the *TTC* plane. The modulation frequency is synchronized with the acquisition frequency. The modulation is performed via an appropriate duty cycle, which decreases the signal-to-noise ratio (*SNR*) (Bensalem [31]). The duty cycle represents the ratio between the duration of excitation over a period and the duration of the period.

2.2. Processing method

The recorded infrared films were processed to obtain the amplitude image for each film and enhance the image quality. The four-image algorithm is used to extract the amplitude of a modulated signal blurred in noise (Rampnoux et al. [32]). The four-image method consists of calculating the sum of a signal for each quarter of a period (*T/4*). The four sums are then used in an amplitude estimation. This method allowed us to obtain the best quality in a short processing time compared to other methods (Bensalem [31]).

An additional image processing method, such as the *SVD*, is used. The *SVD* method reduces the effect of noise and reconstructs amplitude images without high-frequency noise (singular modes). This technique showed an interesting efficiency in noise processing of *3D* complex-valued data in optical diffraction tomography (Shevkunov et al. [33]). The singular values used to reconstruct the amplitude images in this study are 6 values. Other singular values were deleted with their corresponding columns in U and V^T. This allowed to reduce data through reducing significantly the size matrices U, S and V.

Once the images of the amplitude of the transmitted signal are processed, the transmittance can be calculated by dividing the transmitted signal through sample $I(z, y, t)$ by the transmitted signal through the semitransparent enclosure without sample $I_0(z, y)$.

$$Tr = \frac{I(z, y, t)}{I_0(z, y)} \tag{1}$$

The difference between the transmittance issued from raw transmitted signal and transmittance issued from denoised signal by *SVD* allows the obtaining of the noise image situated between −0.05 and +0.01 with an average of −0.02.

When the images of transmittance $Tr(z, y, t)$ are obtained, the space-time field can be obtained through an average transmittance at different positions of y_i. This averaging can be justified by the homogeneous material and the considered homogenous excitation along y at $z = 0$. This can be expressed by the following equation.

$$\overline{Tr(z, t)} = \frac{\sum_{i=1}^{ym} Tr(z, y_i, t)}{ym} \tag{2}$$

ym represents the number of lines between $y = +l$ and $y = -l$.

The conversion of transmittance images $T(z, y, t)$ to the averaged transmittance $\overline{T(z, t)}$ is shown in Fig. 4.

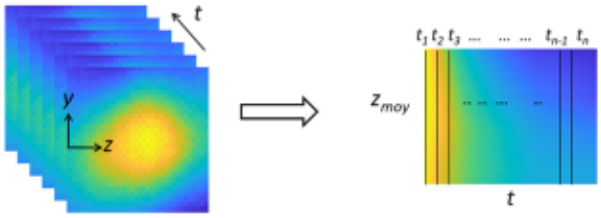

Fig. 4. Example showing the principle of averaging images (z, y, t) to space-time images (z, t) using Eq. (3).

The obtained space-time field of transmittance represents the experimental transmittance that will be used to obtain the water content field. The experimental water content field will be used with an appropriate model allowing the estimation of the diffusion coefficient of the blotting paper along the z-axis.

In this study, we present the space-time field of transmittance to avoid confusing the reader since it represents the appropriate data for the rest of the paper.

The absorbence is defined as the logarithm of the transmitted signal divided by the emitted signal (without sample). Therefore, the averaged absorbence A is given by Eq. (3).

$$A = -\log\left(\overline{Tr(z,t)}\right) \tag{3}$$

3. Diffusion modelling and diffusion coefficient estimation

3.1. Water content imaging under hydric excitation

As indicated previously, in the experiments the excitation is set with low-velocity saturated wet air from one side at $z = 0$. Since the diffusion is supposed to be one-dimensional along the z direction and the signal $I_0(z, y)$ represents the transmitted signal through the enclosure without sample, the averaged transmittance and absorbence over time computed by Eqs. (1), (2) and (3) are summarized in Fig. 5.

Fig. 5-a shows that initially (early in the experiment), the transmittance is maximum along the z-axis, which means that the sample was dry. Over time, the signal decreases, which indicates that the vapour diffuses within the sample. However, the decrease in signal is not the same along z, which is predicted because the closer the position along z to 0, the wetter the area. This can be seen later in the experiment where the zone of z close to 0 is more attenuated.

The absorbence presented in Fig. 5-b shows that initially, the absorbence is low and homogeneous along the z-axis, with the absorbence then becoming higher with diffusion within the sample.

This feature was expected since that one of the main characteristics of terahertz waves is they are attenuated by water content at its liquid or vapour form. Since the experiment are conducted in transmission mode, the signal decreases over the time during wetting the sample. This decrease is exponential with the transmittance according to Beer-Lambert law. This law assumes that the wet sample consists of two layers: one dry layer having the same dimensions of the sample and virtual layer of water having the same surface of the sample and equivalent thickness.

On the other hand, the absorbence representing the absorbed part of signal with respect to the initial signal I_0, it is nothing but the negative logarithm of the transmittance (Eq. (3)).

Therefore, the relationship linking the absorbence and the water content is linear and shown in (Bensalem et al. [27]) by the equation below.

$$\frac{A}{l_s} = \frac{-\log\left(\frac{I(\lambda)}{I_0(\lambda)}\right)}{l_s} = \mu_s + \rho_s \cdot \frac{\mu_w}{\rho_w} \cdot W \tag{4}$$

Thus:

$$W = \frac{\rho_w}{\rho_s \cdot \mu_w} \left(\frac{A}{l_s} - \mu_s\right) \tag{5}$$

with:

ρ_s : Density of blotting paper given by 243 kg/m^3.
ρ_w: Density of water given by 1000 kg/m^3.
μ_s: Absorption coefficient of solid 87 m^{-1}.
μ_w: Absorption coefficient of water 10,000 m^{-1}.
l_s : Thickness of sample 2×10^{-3} m.

By applying Eq. (5), the space-time image of the water content is obtained and given in Fig. 6.

As shown in Eq. (5), the water content field is proportional to the absorbence field. A similarity can be noted with a maximum water content of 16×10^{-3} kg of water /kg of solid. At the beginning of diffusion, the sample is dry (less than 10^{-3} kg of water /kg of solid) since it was placed inside an oven for 24 h. Then, the water content increases with time due to the diffusion of vapour with the material. At $z = 0$ mm, the water content over time is maximal since it represents the first point of contact with the vapour. Fig. 7 shows the diffusion process into the material represented by the evolution of the average water content along z at different times

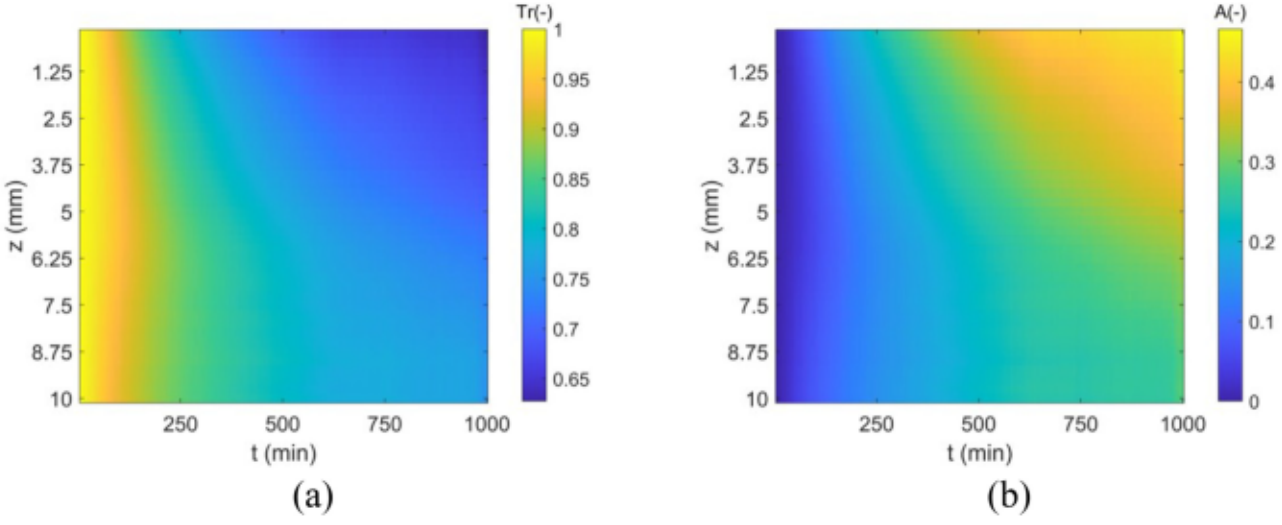

Fig. 5. (a) Image of averaged transmittance, (b) image of absorbence using Eqs. (1)–(3).

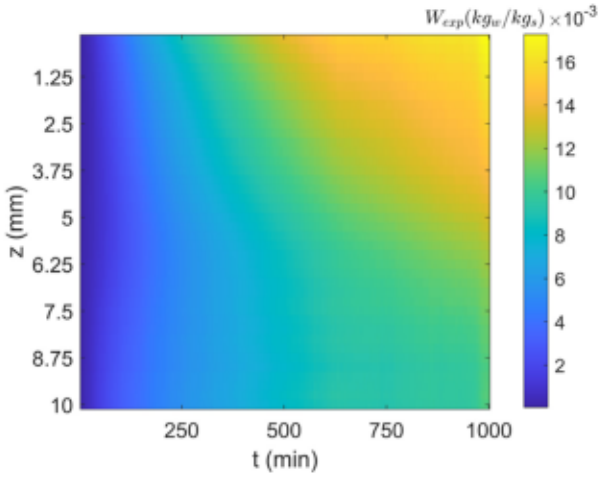

Fig. 6. Experimental space-time field of water content along z within blotting paper.

and the average water content at different positions as a function of time.

Fig. 4-23-a shows that after $z = 5$ *mm*, the mass diffusion of water vapour is low relative to the zone between $z = 0$ *mm* and $z = 5$ *mm*, where the dynamics are remarkable. This can be seen in Fig. 4-23-c, where the water content is almost constant and no significant transfer occurs, especially at early times (less than 250 min). Therefore, only the part situated between $z = 0$ *mm* and $z = 5$ *mm* will be considered in the estimation of the diffusion coefficient.

Fig. 7-b shows that the water content increases inside the sample over time and at different positions along the z-axis. At times greater than 600 min, all the profiles of water content slightly change the dynamics and again take the slope of transfer dynamics at times less than 800 min, which can be due to a possible acquisition problem or related to the camera.

3.2. Mathematical modelling

The measurement of the full field of the *THz* transmittance by the camera provides more data about the diffusion due to the ac-

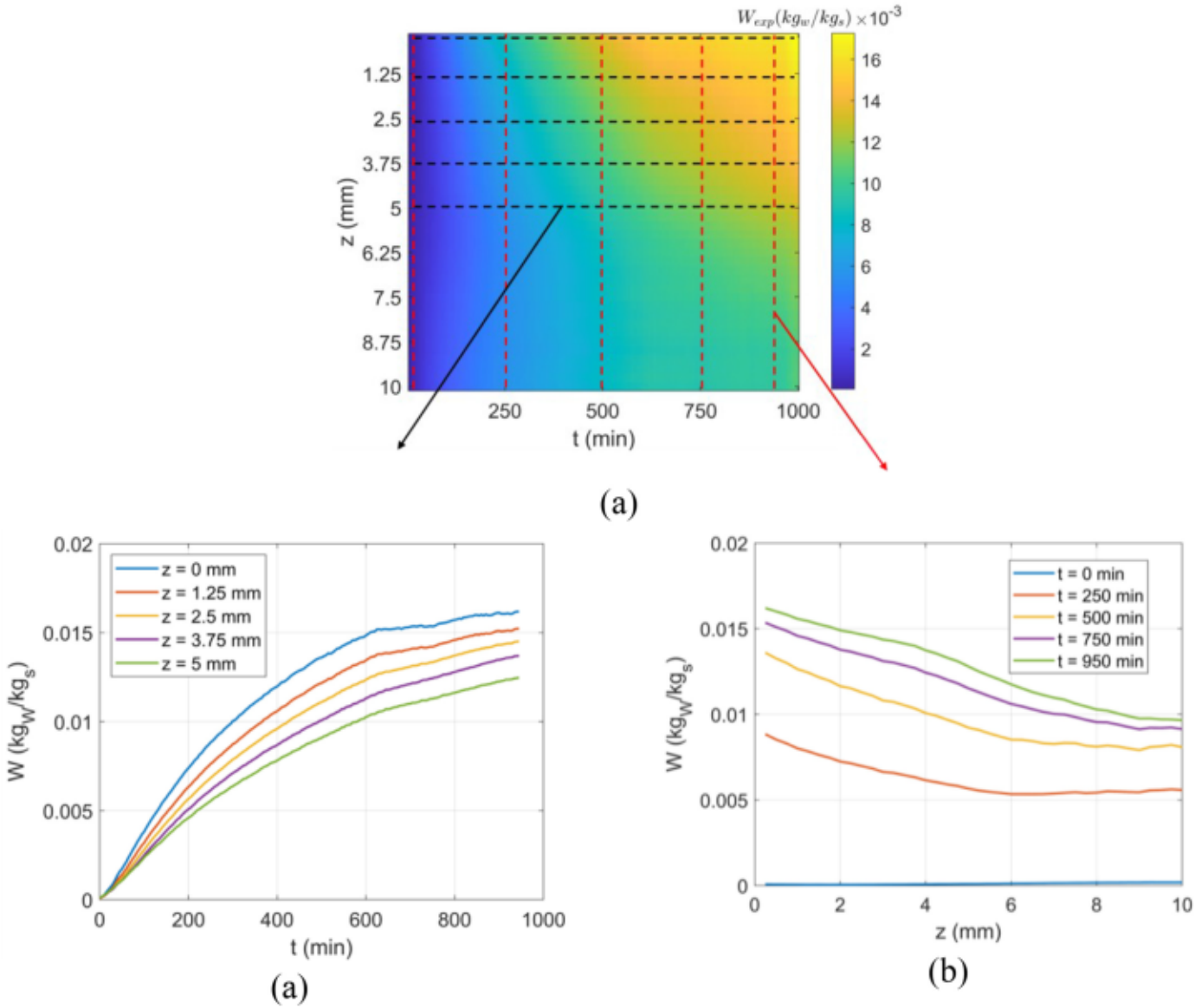

Fig. 7. Profiles of water content (a) at different positions as a function of time, (b) at different instants as a function of z.

quisition rate used (200 *images/s*). Based on the system shown in Fig. 3, several assumptions have been considered in this study:

- The water transfer starts at $z = 0$ and mainly goes through the sample towards the z-axis.
- Due to the low thickness of the sample compared to its in-plane dimensions, we assume that the hydric field is constant along the x-axis for a given z.
- The mass diffusion towards the sample along the z-axis is the same regardless of the value of y (different positions along y). This considers the homogeneity of vapour at $z = 0$ along the y-axis.
- The flux is sufficiently low to eliminate the contribution of the convection coefficient in the boundary conditions of the model. Therefore, the considered boundary condition is the Neumann-type condition, which is a constant water content.
- There is no vapour between the stacked layers of blotting paper.

Considering those assumptions, the mass diffusion will be modelled using a simplified solution of the semi-infinite of Fick's equation. The Fick's second law represents the differential equation of diffusion derived from the Fick's first law assuming that the rate of transfer of diffusing substance through unit area of a section is proportional to the concentration gradient measured normal to the section. Therefore, the ratio of diffusion flux to the opposite of the concentration gradient in the diffusion direction (Crank [34]).

The one-dimensional diffusion process can be described by Fick's law as follows:

$$\frac{\partial W(z,t)}{\partial t} = \frac{\partial}{\partial z}\left(D_z \frac{\partial W(z,t)}{\partial z}\right) \tag{6}$$

Since the material is homogeneous and the excitation along y at $z = 0$ *mm*, the diffusion coefficient D_z can be assumed to be a constant with respect to space, and the expression above becomes:

$$\frac{\partial W(z,t)}{\partial t} = D_z \frac{\partial^2 W(z,t)}{\partial z^2} \tag{7}$$

The boundary conditions in this case can be assumed in this experiment by the following equation.

$$\begin{cases} D_y \frac{\partial W(z,t)}{\partial y}\Big|_{z,y=\pm l} = 0 \\ D_z \frac{\partial W(z,t)}{\partial z}\Big|_{z=L,y} = 0 \\ W(z,t=0) = W(z\to\infty,t) = W_0 \\ W(z=0,t) = W_s \end{cases} \tag{8}$$

Since:

- The material is considered to be homogeneous ($D_z = D_y$).
- The sample is insulated at $y = -l$ and $y = +l$.
- The excitation is considered homogeneous along the left side ($y = \pm\, l$, $z = 0$).

The *1D* solution modelling of the diffusion problem within the semi-infinite assumption is then considered and is given by the equation below:

$$\bar{W} = \frac{W_z - W_0}{W_s - W_0} = erf\left(\frac{z}{2\sqrt{D_z t}}\right) \tag{9}$$

At this stage, the experimental data should be normalized between 0 and 1 to estimate the diffusion coefficient. In the space-time image, the initial water content, which is also the same water content when z tends to infinity (Eq. (8)), represents the last line of the image (line number 20 corresponds to $z = 5$ *mm*), whereas the water content at $z = 0$ is estimated to be the first line of the image. Therefore, the normalized image of the experimental data to be processed is given by the following expression:

$$\bar{W}_{exp} = \frac{Im(z_i,t_j) - Im(z_n,t_j)}{Im(z_1,t_j) - Im(z_n,t_j)}, \quad \begin{matrix} i \to n \\ j \to m \end{matrix} \tag{10}$$

The normalization expression allows the space-time image to be obtained, as shown in Fig. 8.

Fig. 8-a shows that there is a problem with inhomogeneity in the transfer of vapour into the blotting paper early in the experiment. This can be due to the passage of vapour between the 10 stacked blotting papers used in this study (Fig. 2-a). Moreover, at the beginning, there is no pronounced transfer, which allows us to omit the first 50 min from the image corresponding to the first 10 columns (every column represents an averaged image taken every 5 min, as explained previously). Therefore, the obtained exploitable space-time experimental image is shown in Fig. 8-b. Some profiles of the normalized experimental water content are obtained and shown in Fig. 9.

3.3. Estimation method

To estimate the diffusion coefficient based on the model described by Eq. (9), the normalized water content is given as a function of the diffusion coefficient and space-time field. Mathematically, there are different ways to estimate the diffusion coefficient.

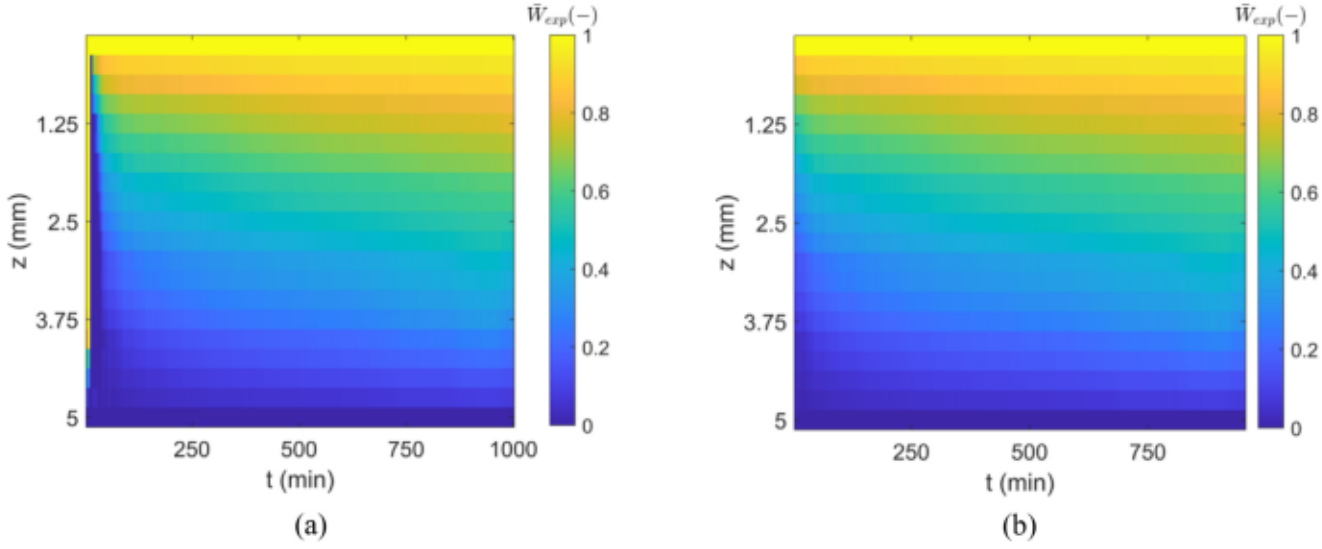

Fig. 8. (a) Normalized water content with anomalies early in the experiment, (b) normalized water content after omitting the anomalies.

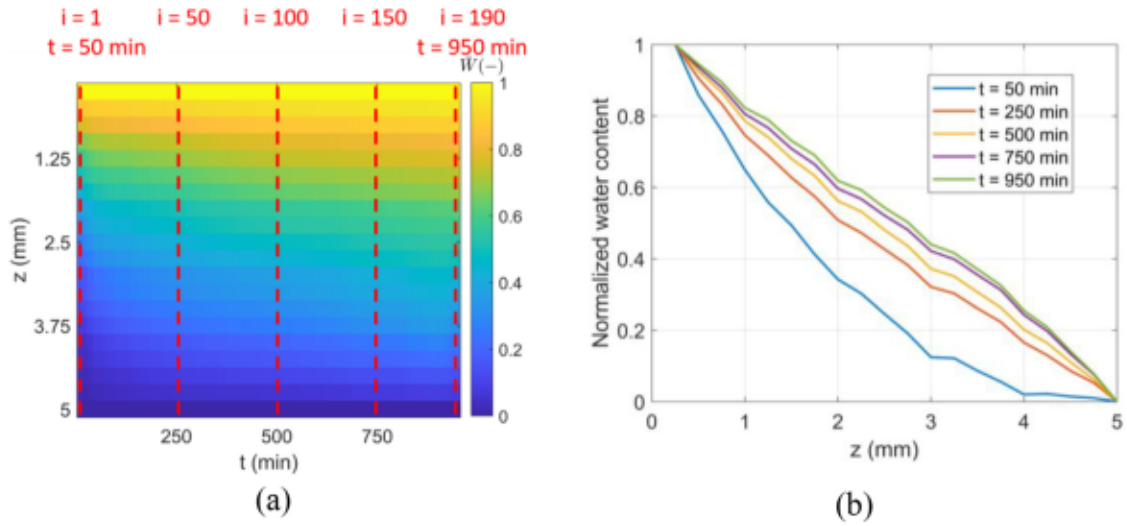

Fig. 9. (a) Normalized water content field with positions of represented profiles, (b) profiles of normalized water content at different instants.

We propose here two methods to estimate the diffusion coefficient: a statistical approach method and a nonlinear minimization inverse method via the software MATLAB®.

3.3.1. Inverse method based on Bayesian approach

This approach consists of modelling the direct problem by reconstructing a database of normalized water content at different values of the diffusion coefficient. Then, the experimental data will be linked to the modelled data through a likelihood function. Thus, the Bayesian inferences are formulated in (Groz et al. [35]) as shown below:

$$P_{posterior}\left(\alpha|\bar{W}(z,t)\right) = \frac{P\left(\bar{W}(z,t)|\alpha\right).P_{prior}(\alpha)}{P\left(\bar{W}(z,t)\right)} \tag{11}$$

$P_{posterior}(\alpha|\bar{W}(z,t))$: Posterior probability density.

$P_{prior}(\alpha)$: Prior density.

$P(\bar{W}(z,t)|\alpha)$: Likelihood function of different water content measurements.

$P(\bar{W}(z,t))$: Marginal probability density of measurement.

For any given value of parameter α to estimate for each pixel (z) at any time (t), the normalized water content can be evaluated. If the correct space and time scale is created, then the fields of water content can be obtained and compared with the experimental values. To optimize the estimation in terms of estimation time, the values of the estimator (the diffusion coefficient in this case is D_z) can be taken between two limits covering the range of the diffusion process within homogeneous hygroscopic material such as blotting paper. Thus, the posterior probability density is related to the likelihood function, as shown in Eq. (12).

$$P_{posterior}\left(\alpha|\bar{W}(z,t)\right) \propto P\left(\bar{W}(z,t)|\alpha\right),\ \alpha \in [\alpha_{min} \dots \alpha_{max}] \tag{12}$$

The likelihood function $P(\bar{W}(x,t)|\alpha)$ is defined by:

$$P\left(\bar{W}(x,t)|\alpha\right) \propto e^{-\frac{1}{2\Gamma^2}\|\bar{W}_{exp}(z,t)-\bar{W}(\alpha,z,t)\|_2^2},\ \alpha \in [\alpha_{min} \dots \alpha_{max}] \tag{13}$$

where:

$\bar{W}(\alpha,z,t)$: Water content estimated using the direct model in Eq. (9).

$\bar{W}_{exp}(z,t)$: Experimental normalized water content obtained using Eq. (10).

First, a discretization of the diffusion coefficient was performed on a logarithmic scale. This can be justified by the equal distribution of discretization for each decade, which allows acceptable sensitivity from decade to decade (one decade is discretization between 10^n and 10^{n+1}). The diffusion coefficient limits are set between 10^{-10} m^2/s and 10^{-7} m^2/s with 30 steps. This means 10 values are given for each decade. The logarithmic distribution of values is shown in Fig. 10.

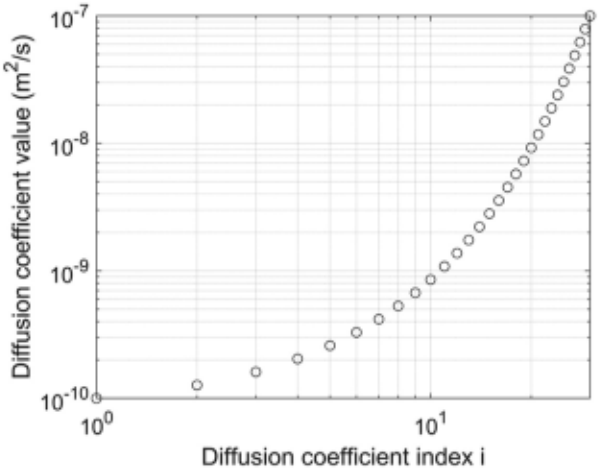

Fig. 10. Logarithmic scale of diffusion coefficient base with 30 points.

Therefore, 30 normalized space-time images will be modelled using discretized values of the diffusion coefficient (D_i) and the space (z) and time (t) scales of the experimental image. The water content fields obtained at different values of the diffusion coefficient ($D_{i=1} = 1 \times 10^{-10}$ m^2/s, $D_{i=10} = 8.53\times10^{-10}$ m^2/s, $D_{i=20} = 9.24\times10^{-9}$ m^2/s and $D_{i=30} = 1 \times 10^{-7}$ m^2/s) are given in Fig. 11.

Fig. 11 shows that at low values of the diffusion coefficient, diffusion can be captured (Fig. 11-a). However, for greater values, the diffusion phenomenon is fast and almost equal to that earlier in the experiment (Fig. 11-c and d). This is due to the space and time scales used. However, keeping the space and time used in the experiment constant, this indicates that the diffusion coefficient that will be obtained is situated close to the diffusion coefficient used to obtain Fig. 11-a and b.

The probability function was computed based on a simple comparison between the quadratic error between the experimental and the modelled (computed) water content fields estimated at different diffusion coefficients. The error here is defined by the differ-

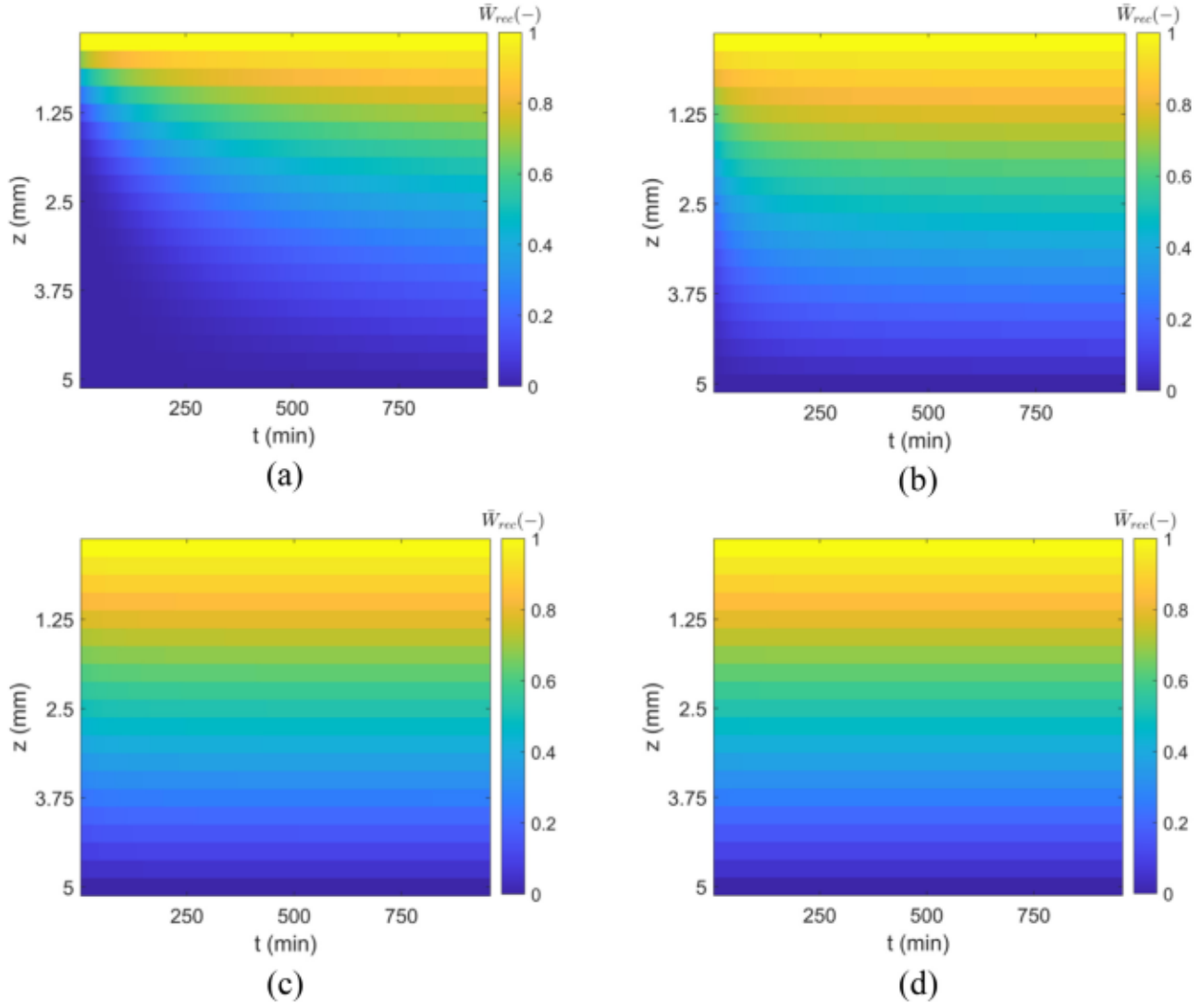

Fig. 11. Water content modelled (reconstructed) at different diffusion coefficients: (a) $D_{i=1} = 1 \times 10^{-10}$ m^2/s, (b) $D_{i=10} = 8.53 \times 10^{-10}$ m^2/s, (c) $D_{i=20} = 9.24 \times 10^{-8}$ m^2/s and (d) $D_{i=30} = 1 \times 10^{-7}$ m^2/s.

ence between the experimental and modelled water content fields. The probability presented by the (Groz et al. [35]) function represents the inverse of the exponential of these quadratic errors and is given by Eq. (14).

$$f_{prob} = e^{-\|W_{exp}(z,t) - W(D_i,z,t)\|_2^2}, \; D_i \in \left[10^{-10} \ldots 10^{-7}\right] \tag{14}$$

The probability function is presented in Fig. 12.

Fig. 12 shows that the maximum in the probability function is obtained at $D_{i=9} = 6.723 \times 10^{-10}$ m^2/s. At this value of diffusion, the estimated water content field is predicted to be the field closest to the experimental field. In this case, it is important to display the experimental and modelled water content fields. Moreover, the error between the two fields can give an indication of both the efficiency of the estimation method and the statistical distribution of error. The fields of water content and error are summarized in Fig. 13.

Fig. 13-a and b show a similarity between the experimental and modelled water content fields. However, a slight difference can be seen at $t < 400$ min and on a position situated between 1 mm and 3 mm. The difference is also seen at z situated between 3 mm and 5 mm for a long time ($t > 700$ min). The error shown in Fig. 13-c is situated between -0.06 and 0.1, which means that the scale of the obtained error is 6% to 10% with respect to the scale of the normalized water content fields.

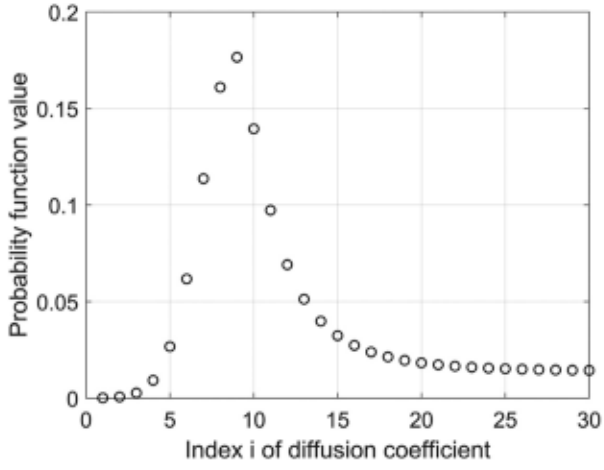

Fig. 12. Probability function at different diffusion coefficients used in water content modelling.

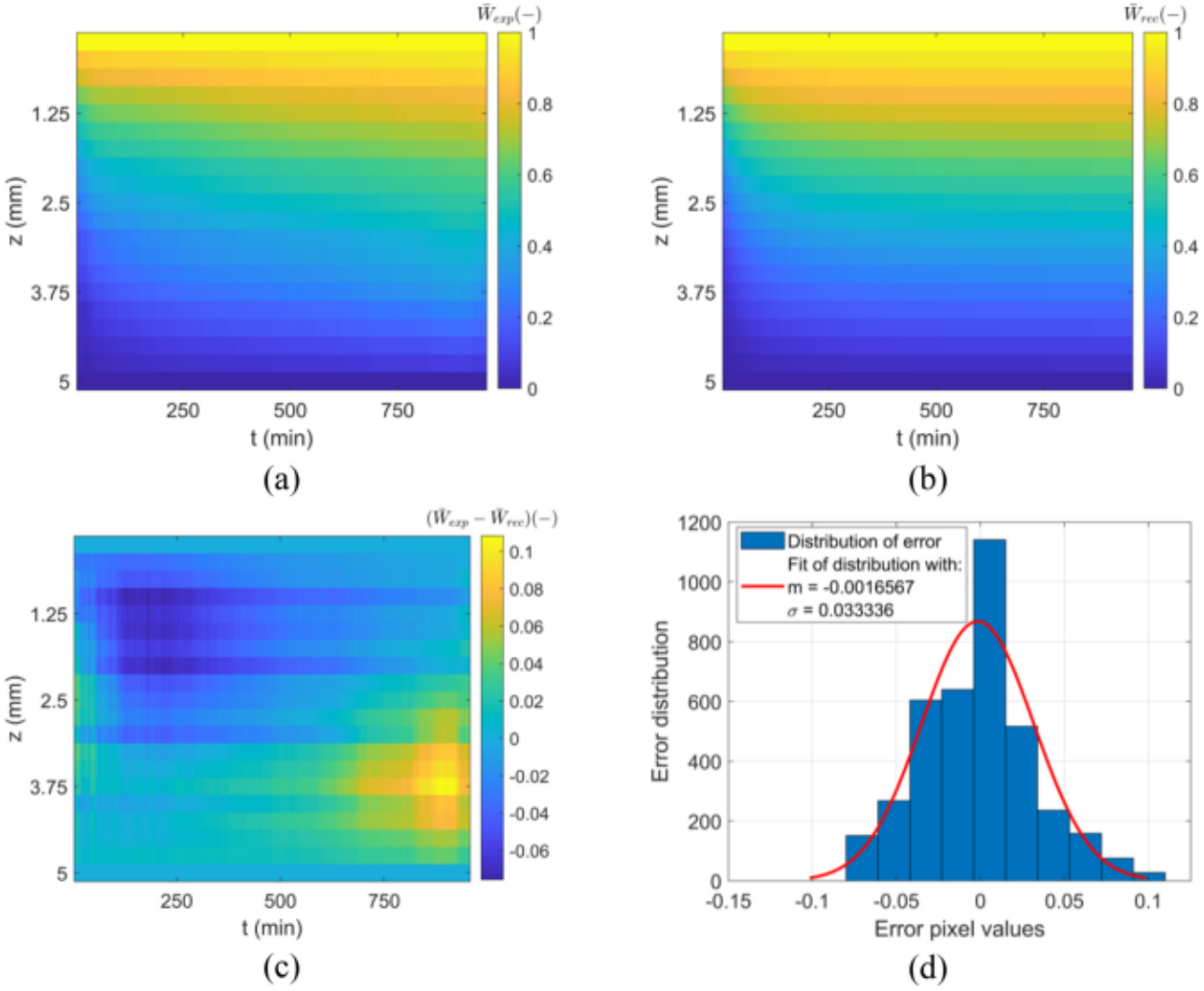

Fig. 13. (a) Experimental water content, (b) modelled water content with $D_{i=9} = 6.723\times10^{-10}\ m^2/s$, (c) difference between the experimental and modelled normalized water content (error), (d) distribution of error with Gaussian fit.

The error can be presented in the form of a histogram with a Gaussian fit to estimate the mean value and the deviation of the error in all the images. The mean value of error is close to 0 and equal to −0.001, while the standard deviation obtained is 0.033. This means that with a diffusion coefficient of $D_{Bayes} = 6.723\times10^{-10}\ m^2/s$, almost 97% of pixels of the modelled water content represent an almost null difference with the experimental field.

To improve the estimation, a refined discretization of the diffusion coefficient based on 1000 values in the same range ($10^{-10}\ m^2/s$ to $10^{-7}\ m^2/s$) is performed. The maximum probability function, corresponding to the minimum difference between the modelled and experimental water contents, is obtained at $D_{i=270} = 6.424\times10^{-10}\ m^2/s$. This value is 5% less than the previous value obtained with 30-point discretization.

Refining the discretization of the diffusion coefficient from 30 points to 1000 points slightly improves the estimation of the water content field. This estimation provides an adjustment of 5% of the diffusion coefficient. However, the computation time is increased 26 times from 0.6 *s* to 15.6 *s*.

However, more robust methods based on the minimization of this quadratic error are necessary and allow the validation of the estimated diffusion coefficient with a statistical fast approach based on Bayesian. For this, an inverse method based on Marquart-Levenberg-based minimization is used in the next paragraph.

3.3.2. *Inverse method based on the Marquart-Levenberg minimization approach*

As mentioned, a simple fast method based on statistical comparison of the error allowed us to estimate a value of the diffusion coefficient of $D_{Bayes} = 6.424\times10^{-10}\ m^2/s$.

In this part, we propose a method based on the minimization of quadratic error using a robust method called the Levenberg–Marquardt (*LM*) algorithm. The algorithm is optimized and allows solving nonlinear least squares problems. The minimization problem arises especially in least squares curve fitting. It interpolates between the Gauss–Newton algorithm and the method of gradient descent. The Levenberg–Marquardt algorithm is more robust for a reasonable starting parameter than the Gauss–Newton algorithm, but it tends to be slower. This method is used to estimate a given parameter β_i of the function $f(z, t, \beta)$ so that the sum of the squares of the deviations $S(\beta)$ is minimized. The estimator can be expressed by Eq. (15).

$$\hat{\beta} \in argmin_{\beta} \sum_{i=1}^{m}\sum_{j}^{n} \left|Y_{i,j} - f\left(z_i, t_j, \beta\right)\right|^2 \tag{15}$$

The algorithm is an iterative procedure that consists of evaluating the model with a starting parameter provided by the user and minimizing the quadratic error between the model at a given position at a given time and the experimental data. In each iteration, the parameter vector β (value in our case) is replaced by a new estimate $\beta+\delta$. To determine variation δ, the function $f(z_i,\ t_j,\ \beta+\delta)$ is approximated by its linearization.

$$f(z_i, t_j, \beta+\delta) = f(z_i, t_j, \beta) + \delta J_{i,j} = f(z_i, t_j, \beta) + \delta \frac{\partial f(z_i, t_j, \beta)}{\partial \beta} \tag{16}$$

The sum of square error $S(\beta)$ has its minimum at the null gradient; thus, the first-order approximation of $f(z_i,\ t_j,\beta+\delta)$ is given in Eq. (17).

$$S(\beta+\delta) \approx \sum_{i=1}^{m}\sum_{j}^{n} \left| Y_{i,j} - f(z_i, t_j, \beta) - \delta J_{i,j} \right|^2 \tag{17}$$

With the $J_{i,j}$ represents the Jacobian matrix. The matrix form can be given as follows.

$$S(\beta+\delta) \approx S(\beta) - 2[Y - f(\beta)]^T J\delta + \delta^T J^T J\delta \tag{18}$$

If the derivative of $S(\beta+\delta)$ with respect to δ is equal to zero, the minimum value can be found by solving the following equation.

$$\left(J^T J\right)\delta = J^T[Y - f(\beta)] \tag{19}$$

In Levenberg-Marquardt method, the adjustment of parameter β is based on the adjustment of another positive parameter called the damping factor λ at each iteration. The value of λ can be initialized by the max of diagonal values of the Hessian matrix. However, its value will be changed at each iteration function of a multiplicator factor that allows the acceleration of the convergence. This parameter will not be further discussed in this paper to avoid confusing the message of the article. This factor can be used in Tikhonov regularization, which is used to solve linear ill-posed problems and it is introduced in the Eq. (20) as follows.

$$\left(J^T J + \lambda Id\right)\delta = J^T[Y - f(\beta)] \tag{20}$$

where Id is the identity matrix and δ is the variation or the increment used to estimate the parameter vector β. In this case, the norm 2 of the error (difference between the two fields) in every iteration will be fed to the algorithm. This aims to calculate the derivative with respect to the parameter β (diffusion coefficient) in every iteration and therefore, updating the value of variation δ of the parameter to estimate β.

The initial parameter is an important parameter in some inversion problems where many local minima are possible. The initial parameter used should be on the same order of magnitude as the diffusion coefficient found with the Bayesian approach. The initial parameter given to the algorithm is $D_0 = 1 \times 10^{-10}\ m^2/s$.

The estimated value by the *LM* algorithm is $D_{minim} = 5.903\times10^{-10}\ m^2/s$. This value represents 8% less than the value found by the Bayesian approach ($D_{Bayes} = 6.424\times10^{-10}\ m^2/s$). The modelled space-time field of normalized water content obtained using this value is shown with the error field and its distribution in Fig. 14.

The error field (Fig. 14-c) shows that the difference between the experimental and modelled fields of water content in the same range found with the diffusion coefficient estimated by the Bayesian approach. The values are slightly different (between −0.06 and 0.1). The mean value obtained here is close to 0 and equal to 0.0029, and the standard deviation of the distribution is 0.032. The lower value of the standard deviation shows that with this value of the diffusion coefficient, there are more pixels of the modelled water content field that have values close to those of the experimental field. This led to 8% of the refined estimated value.

The diffusion coefficient obtained with the Levenberg–Marquardt algorithm, which is an optimized algorithm based on the computation of the derivation of the quadratic error coupled with the parameter of accelerating the convergence through the damping factor, takes a longer time. However, the Bayesian approach represents a fast method based on a computation of the probability function, which is nothing other than a comparison of quadratic errors provided by the difference between the experimental and modelled fields. The obtained value shows that this method is efficient in estimating the diffusion coefficient. The estimated diffusion values in both methods are on the order of magnitude of the diffusion coefficient of cellulose obtained in the literature. The diffusion coefficients are comparable to the modelled values by (Desrosiers [36]), which are $22.4 \times 10^{-10}\ m^2/s$ and the reported value by (Ek et al. [37]), which is $16\times10^{-10}\ m^2/s$.

The difference can be attributed to the considered assumptions, including neglecting the effect of the exchange coefficient with vapour on the boundary condition for simplification. The diffusion coefficient in this study is also considered to be constant, which is not the case in reality. The diffusion coefficient is often taken as a function of the diffusion coefficient of the material at the initial water content and the water content concentration. This relation is given by an exponential expression by (Mannes [38]).

Since the *THz* technique coupled with appropriate processing and estimation methods allowed the obtaining of interesting results, an attempt to extend this estimation method to a heterogeneous material such as wood is carried out. However, it should be mentioned that due to the wavelength size of the source ($\approx$ 2.7 *mm*), which is greater than the width of the growth ring of wood, it is not expected to visualize the rings. Moreover, since the growth rings have different densities (earlywood and latewood), the diffusion coefficient will certainly differ from ring to other. Therefore, the average of images along the *y*-axis will allow us to estimate only the average longitudinal diffusion coefficient of maritime pine (Pinus pinaster).

3.4. Application to the heterogeneous material maritime pine

In this part, the same experiment conducted on blotting paper is performed on a maritime pine sample in the tangential longitudinal direction with a thickness of 2 *mm*. The setup is shown in Fig. 15.

It is worth recalling that along the *z* direction, the diffusion coefficient may not be constant due to growth ring alternation within the wood. This leads us to assume that the averaging of transmittance images will lead to an averaged apparent diffusion coefficient along the *z*-axis. This averaging leads to simplification of the *2D* transient model to a *1D* transient model, which joins the previous study carried out on a homogeneous material.

The estimation has been set using the approaches explained above (Bayesian and minimization method). The obtained values of the diffusion coefficient are:

Bayesian approach: $D_{Bayes\text{-}wood} = 3.905\times10^{-10}\ m^2/s$.
LM algorithm minimization: $D_{minim\text{-}wood} = 3.772\times10^{-10}\ m^2/s$.

The diffusion coefficients found for maritime pine during the wetting process are specific to the direction studied (longitudinal). Literature on the diffusion coefficient of wood, obtained through various techniques, shows significant variation depending on the species, such as tropical species (Perre et al. [39]), spruce (Mouchot et al. [40]), beech (Mouchot et al. [41]), and pine (Siau [42]), as well as the direction of diffusion, whether it's a permanent or transient process, and whether it's drying or wetting.

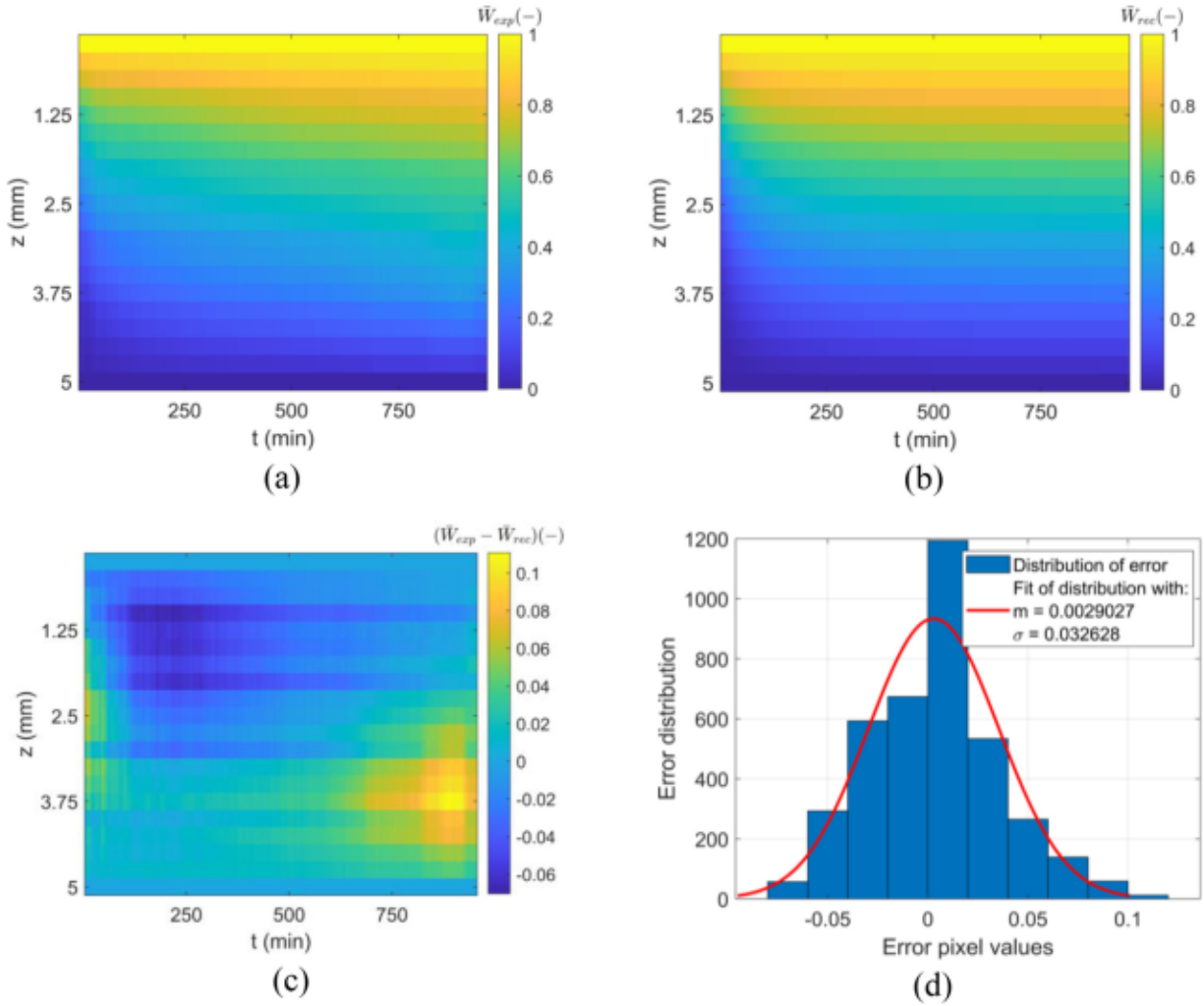

Fig. 14. (a) Experimental water content, (b) modelled water content with $D_{mism} = 5.903 \times 10^{-10}$ m^2/s, (c) difference between the experimental and modelled normalized content (error), (d) distribution of error with Gaussian fit.

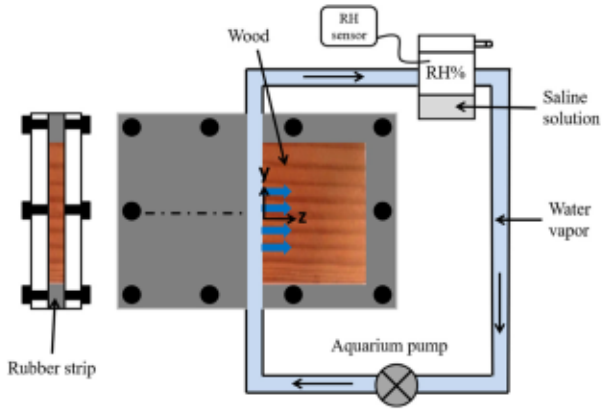

Fig. 15. Hydric excitation of maritime pine sample along the longitudinal direction L (along the ring z-axis).

The following table summarizes some values reported by (Mouchot et al. [41]) provides a summary of values found in the literature on wood diffusion coefficients.

The Table 1 demonstrates that the diffusion coefficient within wood varies greatly, making it difficult to establish a reference value. However, for pine, we find that the diffusion coefficients for the three directions (T, R, and L) are established under steady-state conditions. These values are of the order of 10^{-7} m^2/s, which is significantly different from the diffusion coefficient obtained during a transient process (0.21×10^{-10} m^2/s). This value is closer to the value obtained for pine in the current study (3.772×10^{-10} m^2/s).

Table 1
Values of diffusion coefficients summarized by (Mouchot et al. [41]) obtained in different experimental conditions (temperature and humidity), different directions (T: Tangential, R: Radial, L: Longitudinal, $R + T$: average of the radial and tangential direction), and by different authors.

Species	Diffusion coefficient obtained in steady-state case (m^2/s)	Diffusion coefficient obtained in transient case (m^2/s)	Direction
Fir	3.24×10^{-10}		$R + T$
		2.82×10^{-10}	R
		3×10^{-10}	L
		$4.97\ 10^{-10}$	/
Pine	3.5×10^{-7}		T
	8.04×10^{-6}		L
	4.88×10^{-7}	21.1×10^{-11}	R
			$R + T$
Poplar	9.22×10^{-9}	2.10×10^{-10}	L
		2.60×10^{-6}	R
Oak	1.87×10^{-7}		T
	2.82×10^{-6}		L
	1.85×10^{-7}		R
		1.14×10^{-10}	R
		5.46×10^{-10}	L

Table 2
Values of the global diffusion coefficients obtained for different laminated pine samples during drying summarized by (Clouet [2]).

Species	Global diffusion coefficient for pine (m^2/s)
Sample 1	5.84×10^{-10}
Sample 2	7.47×10^{-10}
Sample 3	9.47×10^{-10}

The difference can be attributed to the direction of diffusion and the process conditions (drying or wetting).

The author (Clouet [2]), has estimated the global value of the diffusion coefficient for different laminated pine samples using Nelder-Mead algorithms as the optimization technique. The results are summarized in Table 2 and report different values for the diffusion coefficient of maritime pine.

The values listed in Table 2 are more in line with the diffusion coefficient found for pine in this study (3.772×10^{-10} m^2/s). The difference can be attributed to two factors: (a) the difference in studied processes, with (Clouet [2]) focusing on drying and this study focusing on wetting, and (b) the estimation method, with (Clouet [2]) estimating the global diffusion coefficient by monitoring the global weight of the sample and this study monitoring the diffusion along the longitudinal direction without contact using *THz* technique.

Despite all, these values allow validating our values of diffusion coefficient obtained for pine and thereby validating our *THz* contactless imaging-based setup and used inverse methods for the estimation. The validity of our estimated diffusion coefficients for pine can be confirmed by comparing the average experimental water content field with the reconstructed field using the estimated value. By measuring the difference between the two fields, we can determine the accuracy of our *THz* contactless imaging setup and inverse methods. The results, including the experimental field, the modelled field using the diffusion coefficient from the *I.M* algorithm, and the error between them, are displayed in Fig. 16.

As shown in Fig. 16-a, the diffusion within wood includes some problems early in the experiment, which can be attributed to the heterogeneity of wood that involves more noise with infrared images and more heterogeneity in the distribution of water content. The modelled water content field obtained with a diffusion coefficient of 3.772×10^{-10} m^2/s shows a similar space-time field of water content to the experimental field (diffusion dynamics, characteristic time, diffusion depth). However, the error indicating the difference between the experimental and the modelled fields is situated between −0.1 and 0.1 with an important gap early in the experiment up to 0.25. The distribution of error shows that the mean error is close to 0 and equal to −0.001 with a standard deviation of 0.046. The standard deviation of the error is one and one-half

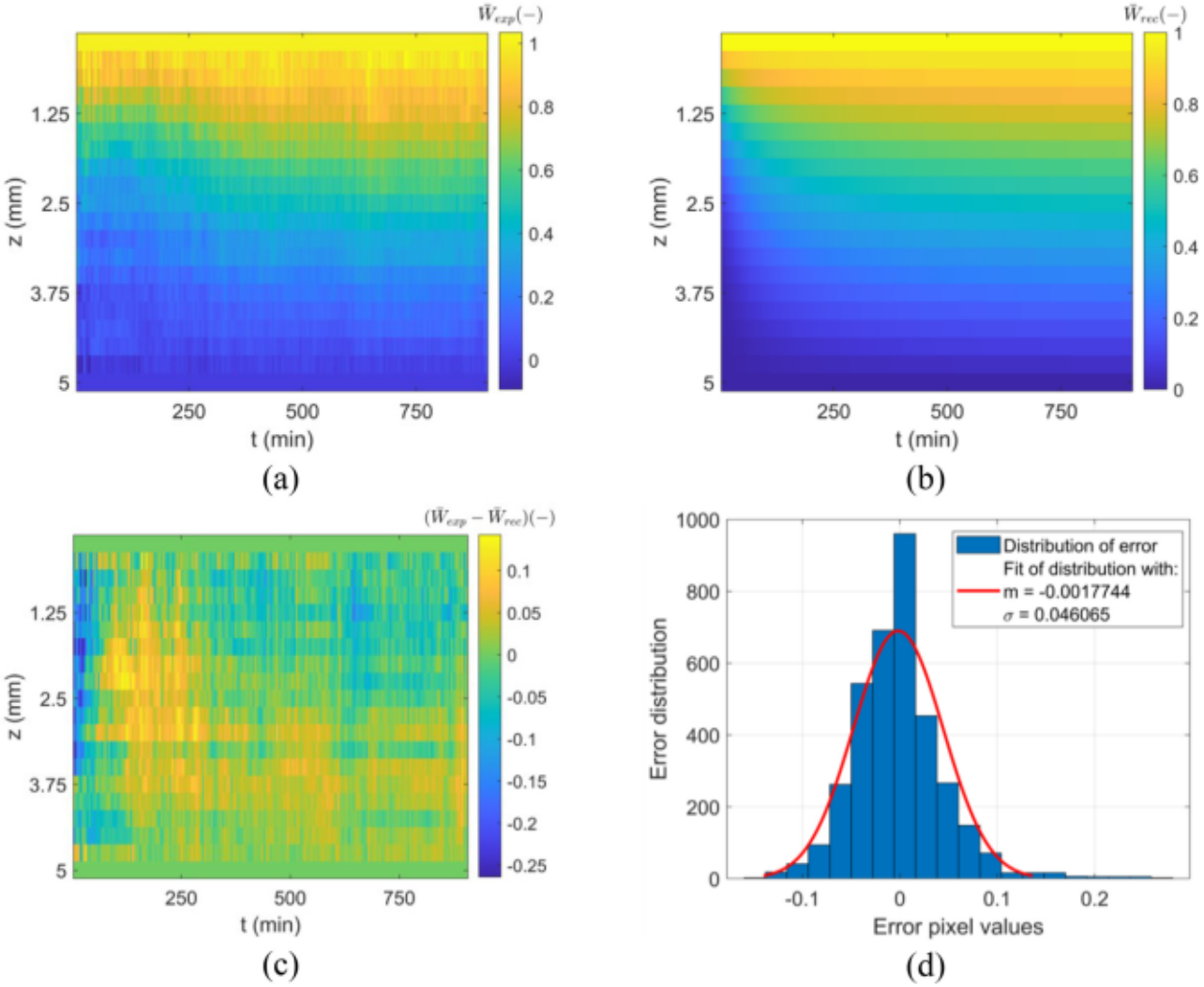

Fig. 16. (a) Experimental water content of wood, (b) modelled water content with $D_{\text{mism-wood}} = 3.772\times10^{-10}$ m^2/s, (c) difference between the experimental and modelled normalized content (error), (d) distribution of error with Gaussian fit.

times that obtained in the case of blotting paper. This can be predicted due to the alternation of different density-growth rings. In fact, within wood, diffusion along the *y*-axis is different from diffusion along the *z*-axis, and diffusion along the *z*-axis is different from earlywood growth rings to latewood growth rings. This induces different diffusion along the *z*-axis as a function of the position of *y;* thus, the obtained images were noisy relative to images showing diffusion within a homogeneous material. Moreover, it can be noted that with the same scale time, the diffusion depth is lower, which intuitively means that the diffusion coefficient of wood would also be lower.

4. Conclusions and perspectives

The aim of this study was to show the efficiency of *THz* imaging for contactless characterization of transient water vapour diffusion in hygroscopic materials. The study was conducted on two hygroscopic materials: homogeneous (blotting paper) and heterogeneous (maritime pine). The results were comparable to literature values, with the obtained diffusion coefficient for blotting paper and pine being 5.93×10^{-10} m^2/s and 3.77×10^{-10} m^2/s, respectively, compared to values of 16×10^{-10} m^2/s and 5.84×10^{-10} m^2/s in the literature. This demonstrates the capability of *THz* imaging to monitor transient water vapour diffusion without contact. The differences with literature can be attributed to various factors, including the studied process, regime, used methods, boundary conditions, etc.

The error between the experimental and modelled average water content was between −6% and +10% for blotting paper and ±10% for maritime pine. The inverse method using the *LM* method showed a higher accuracy of 8% compared to the Bayesian statistical approach. However, the latter had a shorter computation time, taking one-third of the time required by the former in our case.

This study is of great significance from an industrial perspective. This is because water content diffusion is a crucial factor in the paper and wood industries, particularly during the humidification or drying phases, which has a direct impact on the final product quality.

Scientifically, this study lays the foundation for exciting advancements by combining *THz* technology for monitoring water content field and digital image correlation (*DIC*) for monitoring mechanical properties field during the drying or wetting of hygroscopic materials.

Potential advancements for this study include:

- Incorporating convection in boundary conditions.
- Evaluating the estimation for varying growth ring directions in wood.
- Experimenting with alternative excitations such as Dirac pulses and adapting estimation methods from heat transfer to mass transfer, such as the parabolic method.

It is important to note that the low power of the source restricts the system to thin wood samples, primarily wet samples. *THz* technology holds potential for measurements on dry, less-dense products in other industries such as food and packaging, which typically lack dependable real-time measurements.

Funding

This research received no external funding.

Declaration of Competing Interest

The authors declare that they have no known competing financial interests or personal relationships that could have appeared to influence the work reported in this paper.

CRediT authorship contribution statement

M. Bensalem: Conceptualization, Methodology, Software, Validation, Formal analysis, Investigation, Investigation, Resources, Data curation, Writing – original draft, Writing – review & editing, Visualization, Supervision, Project administration, Funding acquisition. **A. Sommier:** Conceptualization, Methodology, Software, Validation, Formal analysis, Investigation, Resources, Data curation, Writing – original draft, Writing – review & editing, Visualization, Supervision, Project administration, Funding acquisition. **J.C. Mindeguia:** Conceptualization, Methodology, Software, Validation, Formal analysis, Investigation, Investigation, Resources, Data curation, Writing – original draft, Writing – review & editing, Visualization, Project administration, Funding acquisition. **J.C. Batsale:** Conceptualization, Resources, Methodology, Validation, Formal analysis, Investigation, Data curation, Writing – original draft, Writing – review & editing, Visualization, Supervision, Project administration, Funding acquisition. **C. Pradere:** Conceptualization, Methodology, Software, Validation, Resources, Investigation, Data curation, Writing – original draft, Writing – review & editing, Visualization, Supervision, Project administration, Funding acquisition.

Data availability

No data was used for the research described in the article.

Supplementary materials

Supplementary material associated with this article can be found, in the online version, at doi:10.1016/j.ijheatmasstransfer.2023.124064.

References

[1] B. Clouet, R. Pommier, M. Danis, New composite timbers, full field analysis of adhesive behavior, in: Proceedings of the Part of the series Conference Society for Experimental Mechanics Series pp, 2013, pp. 51–58. 14 August.

[2] B. Clouet, Comportement Hydromécanique D'assemblages Bois Collés à L'état Vert - Approches Expérimentale et Numérique, University of Bordeaux, 2014 *PhD* thesisMay.

[3] S.V. Dvinskikh, M. Henriksson, A.L. Mendicino, S. Fortino, T. Toratti, NMR imaging study and multi-Fickian numerical simulation of moisture transfer in Norway spruce samples, Eng. Struct. 33 (2011) 3079–3086.

[4] D. Derome, S. Roels, J. Carmeliet, Qualitative Work to Study Water Movement in Wood, Source: Div. of Building Technology /Department of Civil and Architectural Engineering / Royal Institute of Technology, Brinellvägen 34, SE-100 44, Stockholm, Sweden, 2005.

[5] K. Sandberg, Modelling water sorption gradients in spruce wood using CT scanned data, N. Z. J. For. Sci. 36 (2/3) (2006) 347–364.

[6] W. Zillig, Moisture transport in wood using a multiscale approach, PhD thesis of the Catholic University of Louvain, 2009 MayUDC 538.93: 691.11, D/2009/7515/56, ISBN 978- 94-6018-073-6.

[7] S. Hameury, M. Sterley, Magnetic resonance imaging of moisture distribution in pinus sylvestris l exposed to daily indoor relative humidity fluctuations, Wood Mater. Sci. Eng. 1 (2006) 116–126.

[8] M.B. MacMillan, M.H. Schneider, A.R. Sharp, B.J. Balcom, Magnetic resonance imaging of water concentration in low moisture content wood, Wood Fiber Sci. 34 (2) (2002) 276–286.

[9] J. Ekstedt, A. Rosenkilde, S. Hameury, M. Sterley, H. Berglind, Measurement of moisture content profiles in coated and uncoated Scots Pine using Magnetic Resonance Imaging, in: Proceedings of the Conference - Quality Control for Wood and Wood Products, Warsaw, Poland, 2007.

[10] M.S. Gilani, S. Abbasion, E. Lehmann, J. Carmeliet, D. Derome, Neutron imaging of moisture displacement due to steep temperature gradients in hardwood, Int. J. Therm. Sci. 81 (2014) 1–12.

[11] M.S. Gilani, P. Vontobel, E. Lehmann, J. Carmeliet, D. Derome, Moisture migration in wood under heating measured by thermal neutron radiography, Exp. Heat Transf. J. Therm. Energy Gener. Transp. Storage Convers. 27 (2) (2013) 160–179.

[12] S. Abbasion, J. Carmeliet, M.S. Gilani, P. Vontobel, D. Derome, A hygrothermo-mechanical model for wood: part A. Poroelastic formulation and validation with neutron imaging – Cost Action FP0904. 2010-2014: thermo-hydro-mechanical wood behavior and processing, Article Holzforschung (2015) January.

[13] D. Banerjee, W. Von Spiege, M.D. Thomson, S. Schabel, H.G. Roskos, Diagnosing water content in paper by terahertz radiation, Opt. Express 16 (12) (2008) 9060.

[14] S. Hadjiloucas, L.S. Karatzas, J.W. Bowen, Measurement of leaf water content using Terahertz radiation, IEEE Trans. Microw. Theory Tech. 47 (2) (1999) February.

[15] H.B. Zhang, K. Mitobe, N. Yoshimura, Application of terahertz imaging to water content measurement, Jpn. J. Appl. Phys. 47 (10) (2008) 8065–8070.

[16] R. Gente, N. Born, N. Voß, W. Sannemann, J. Léon, M. Koch, E. Castro-Camus, Determination of leaf water content from terahertz time-domain spectroscopic data, J. Infrared Milli. Terahz. Waves 34 (2013) 316–323.

[17] L.G. Santesteban, I. Palacios, C. Miranda, J.C. Iriarte, J.B. Royo, R. Gonzalo, Terahertz time domain spectroscopy allows contactless monitoring of grapevine water status, Front. Plant Sci. 6 (2015) 404 JuneArticle.

[18] C. Jördens, S. Wietzke, M. Scheller, M. Koch, Investigation of the water absorption in polyamide and wood plastic composite by terahertz time-domain spectroscopy, Polym. Test. 29 (2010) 209–215.

[19] R. Piesiewicz, C. Jansen, S. Wietzke, D. Mittlemann, M. Koch, T. Kürner, Properties of Building and Plastic Materials in the *THz* Range, Int. J. Infrared Milli. Waves 28 (2007) 363–371.

[20] M. Bensalem, A. Sommier, J.C. Mindeguia, J.C. Batsale, Luis-David Patino-Lopez, C. Pradere, Contactless transient *THz* temperature imaging by thermo-transmittance technique on semitransparent materials, J. Infrared Milli. Terahz. Waves 39 (2018) 1112–1126.

[21] J.A. Mukam Fotsing, C.W. Tchagang, Experimental determination of the diffusion coefficients of wood in isothermal conditions, Heat Mass Transf. 41 (11) (2005) 977–980.

[22] K. Yasushi, Nondestructive measurement of moisture diffusion coefficient in wood drying, Dry. Technol. 10 (5) (1992) 1231–1248.

[23] H. Koponen, Dependences of moisture transfer coefficients on moisture diffusion coefficients and wood properties, Paper i Ja Puu 6 (1985) 363–368.

[24] J. Eriksson, H. Johansson, J. Danvind, Numerical determination of diffusion coefficients in wood using data from *CT*-scanning, J. Soc. Wood Sci. Technol. 38 (2) (2006) 334–344.

[25] J.Y. Liu, W.T. Simpson, S. Verrill, An inverse moisture diffusion algorithm for the determination of diffusion coefficient, Dry. Technol. 19 (8) (2001) 1555–1568.

[26] P.N. Peralta, A.P. Bangi, A nonlinear regression technique for calculating the average diffusion coefficient of wood during drying, J. Soc. Wood Sci. Technol. 35 (3) (2003) 401–408.

[27] M. Bensalem, A. Sommier, J.C. Mindeguia, J.C. Batsale, C. Pradere, Terahertz measurement of the water content distribution in wood materials, J. Infrared Milli. Terahz. Waves (2017) Nov.

[28] I.L. Animasaun, N.A. Shah, A. Wakif, B. Mahanthesh, R. Sivaraj, O.K. Koriko, Ratio of Momentum Diffusivity to Thermal Diffusivity: Introduction, Meta-analysis, and Scrutinization, Chapman and Hall/CRC, New York, 2022 ISBN-13: 978-1032108520, ISBN-10: 1032108525, ISBN9781003217374, doi:10.1201/9781003217374.

[29] M. Romano, A. Chulkov, A. Sommier, D. Balageas, V. Vavilov, J.C. Batsale, C. Pradere, Broadband sub-terahertz camera based on photothermal conversion and IR thermography, J. Infrared Mill. Terahz. waves (2016) January.

[30] W.J. Parker, R.J. Jenkins, C.P. Butler, G.L. Abbott, Flash method of determining thermal diffusivity, heat capacity, and thermal conductivity, J. Appl. Phys. (1961).

[31] M. Bensalem, Development of Contactless *THz* Imaging of Water Content and Temperature Fields For the Purpose of Thermal and Mass Characterization of Diffusion Coefficients, University of Bordeaux, 2018 PhD thesis, presented October, 08.

[32] J.M. Rampnoux, H. Michel, M.A. Salhi, S. Grauby, W. Claeys, S. Dilhaire, Time gating imaging through thick silicon substrate: a new step towards backside characterization, Microelectron. Reliab. 46 (2006).

[33] I. Shevkunov, M. Ziemczonok, M. Kujawińska, K. Egiazarian, Complex-domain *SVD*- and sparsity-based denoising for optical diffraction tomography, Opt. Lasers Eng. 159 (2022) 107228.

[34] J. Crank, The Mathematics of Diffusion, 2nd ed., Brunel University Uxbridge. Clarendon press. Oxford, 1975.

[35] M.M. Groz, A. Sommier, E.A. Chavanne, S. Chevalier, J.L. Battaglia, J.C. Batsale, C. Pradere, Thermal resistance field estimations from IR thermography using multiscale Bayesian Inference, Appl. Sci. 10 (7) (2020) 2351.

[36] D. Desrosiers, Modélisation Du Transfert De Chaleur Et D'humidité Dans Une Membrane De Cellulose, University of Québec, Trois-Rivières, Montréal, 2009 Maîtrise thesis.

[37] R. Ek, H. Lennholm, R. Davidson, C. Nystrom, G. Ragnarsson, Pore swelling in beads made of cellulose fibres and fibre fragments, Int. J. Pharmaceutics. 122 (1195) (1995) 49–56.

[38] D.C. Mannes, Non-destructive Testing of Wood By Means of Neutron Imaging in Comparison With Similar Methods, Albert-Ludwigs-Universität Freiburg i. Br., 2009 Ph.D thesis.

[39] P. Perre, S. Zohoun, A Brandão, Determination of mass diffusivity in steady state: results of a measurement campaign on different temperate and tropical species, Sciences et Industries du Bois –4th colloquium, 1996 11-12-13 Sept.

[40] N. Mouchot, F. Thiercelin, P. Perre, A. Zoulalian, Characterization of diffusionnal transfers of bound water and water vapor in beech and spruce, Maderas. Ciencia y Tecnol. 8 (3) (2006) 139–147.

[41] N. Mouchot, A. Wehrer, V. Bucur, A. Zoulalian, Détermination indirecte des coefficients de diffusion de la vapeur d'eau dans les directions tangentielle et radiale du bois de hêtre, Ann. For. Sci. 57 (2000) 793–801 © INRA, EDP Sciences.

[42] J.F. Siau, Nonisothermal moisture movement in wood, Wood Sci. 13 (1) (1980) 11–13.